



# Influence of fault zone on the respect distance and margin for excavation: a case study of the F4 fault in the Jijicao rock block, China

Peixing Zhang<sup>1,2</sup> · Xiaozhao Li<sup>1,2</sup> · Zhen Huang<sup>1,3</sup> · Yangsong Zhang<sup>4</sup> · Xihe Yao<sup>1,2</sup>

Received: 14 September 2017 / Accepted: 13 March 2018 / Published online: 2 April 2018  
© Springer-Verlag GmbH Germany, part of Springer Nature 2018

## Abstract

A high-level radioactive waste repository requires a rock mass to have good retardation properties. However, because a fault zone can be a potential seepage conduit for nuclides, its influence on the hydraulic conductivity of that fault zone must be assessed. Key sets of fractures were found based on an assessment of the statistical characteristics of fracture orientations and the tectonic analysis of a representative north–east fault in the Jijicao rock block in the Beishan region of Gansu Province, China. The trace midpoint density of each set was calculated using ArcGIS, a geographic information system, and a model of the hydraulic conductivity in the fault zone was developed based on a water pressure test and calculations, such that the respect distance and margin for excavation of this fault could also be determined. The calculated results show that the fault core and host rock are less conductive when the damage zone is 10- to 100-fold more conductive due to its greater density of fractures. The density is stable at 100 m, while the key set is stable until 65 m, and the calculated hydraulic conductivity is stable until 25 m; these results are consistent with the results of water pressure analysis.

**Keywords** High-level radioactive waste repository · Fault zone · Respect distance · Margin for excavation · Trace midpoint density · Water pressure test · Hydraulic conductivity

## Introduction

The Jijicao rock block in the Beishan region of Gansu Province has been selected as a candidate site for the disposal of high-level radioactive waste (HLW). The structure of the rock mass is uniform and dense, and the Jijicao block is a stable rock mass (Chen et al. 2015). Because HLW contains long-lived radioactive nuclides, there are strict requirements for its disposal. Over time, HLW seeps into the groundwater supply, and its radioactive nuclides will eventually dissolve into groundwater, which

will then migrate into the biosphere and cause harm to both human health and the ecological system; consequently, the seepage field produced by the migration of radioactive nuclides through a fault zone cannot be ignored (Lee and Jeong 2011; Lee and Kim 2016). Compared to intact rock masses, faults and their surrounding areas usually have greater porosity and permeability. The Jijicao rock block has faults and secondary structures that characterize the seepage field. The surrounding area is considered to likely represent a future potential conduit for nuclide transport and, therefore, it plays an important role in determining the suitability of the Jijicao rock block as a site for the disposal of HLW. During the treatment and operation of the Jijicao rock block as an HLW disposal site, radionuclide migration could occur. It is therefore very important and timely to study the range of effects this potential HLW disposal site may have on human health and the ecological system and to determine its layout (Pere et al. 2012; Ishibashi et al. 2016).

The structure and conductivity of a fault zone have important effects on nuclide traps during the operations period of a HLW disposal site (Yoshida et al. 2005, 2013a, b, 2014; Ishibashi et al. 2016). The structure of a fault zone has been widely agreed upon to comprise two parts: the core of the fault, which includes the fault slip surface and fault breccia,

---

✉ Peixing Zhang  
NJUpzx@163.com

<sup>1</sup> School of Earth Sciences and Engineering, Nanjing University, Nanjing, Jiangsu 210093, China

<sup>2</sup> NJU-ECE Institute for Underground space and Geoenvironment, Nanjing University, Nanjing 210093, China

<sup>3</sup> School of Resources and Environment Engineering, Jiangxi University of Science and Technology, Ganzhou 341000, China

<sup>4</sup> Department of Civil Engineering, Nanjing University of Science and Technology, Nanjing, Jiangsu 210094, China

fractured rock and mud, and the damage zone, which includes secondary faults, fractures and fault folds (Chester and Logan 1986; Knipe and Lloyd 1994; McGrath and Davison 1995; Caine et al. 1996; Storti et al. 2003; Molli et al. 2010; Bauer et al. 2015). McCaig (1988) and Sibson (1996) argued that the dominant effects of fault zones are on surface and superficial seepage. It has also been widely accepted that the role of a fault zone may be that of a conduit, a barrier or a combined conduit–barrier structure (Caine et al. 1996; Knipe 1993; Rawling et al. 2001; Storti et al. 2003; Micarelli et al. 2006; Matonti et al. 2012; Walker et al. 2013). Fisher and Knipe (1998) and Doughty (2003) noted that gouges, which control fault seals, reduce permeability along a fault and thus function as sealants for rocks. A similar conclusion was reached by Storti et al. (2003) who analyzed the size distribution of gouge particles. Evans et al. (1997), Haneberg et al. (1999) and Agosta et al. (2007) argued that the permeability of a fault zone may be several orders of magnitude higher than that of the host rock and that the former is clearly the more favorable setting for conducting water. Bruhn et al. (1994) and Caine et al. (1996) reported that the permeability and intensity of fault zones are controlled by both existing and nascent structures, regional stress fields, fault geometries and lithological changes, as well as by forces, heat, seepage, geochemistry and other factors.

The fault deformation zone often strongly influences the transport of fluids through rocks. During the hydrogeological analysis of a deformation zone, the Swedish Nuclear Fuel and Waste Management Company (SKB) found high hydraulic conductivity values ranging from  $1 \times 10^{-4}$  to  $1 \times 10^{-6}$  m/s for the near-surface deformation zone (plastic deformation results in a plastic shear zone and brittle deformation results in a brittle fault zone) and near-horizontal zones. The hydraulic conductivity values measured in other deformation zones ranged from  $1 \times 10^{-4}$ – $1 \times 10^{-6}$  to  $1 \times 10^{-6}$ – $1 \times 10^{-8}$  m/s. Walker and Gylling (1998, 1999) and Andersson (1999) argued that if the hydraulic conductivity is  $10^{-8}$  m/s for only a small part of the rock mass (e.g. on a scale of 30 m), the rock can retard the release of nuclides during the operations period of the repository. These authors also stated that there will be a very large hysteresis effect which will greatly delay the migration of nuclides, with a Darcy flow rate of  $< 0.01$  m/year. In addition, the seepage rate of the treatment hole during the period of disposal must also be controlled so that it is  $<$  than 10 L/min. The hydraulic conductivity of the surrounding rock mass (on a scale of 10–30 m) should not exceed  $10^{-8}$ – $10^{-7}$  m/s (Walker and Gylling 1998, 1999; Andersson 1999). Based on these reports, the SKB suggested that the permeability of the host rock and internal deformation zone are significantly lower than that near the surface close to the horizontal deformation zone. With the injection of cement slurry, the hydraulic conductivity value can be reduced to  $1 \times 10^{-9}$  m/s, and the

hydraulic conductivity value near the surface and close to the deformation zone can be reduced to  $1 \times 10^{-8}$  m/s; that is, a better hysteresis effect can be achieved that will delay the migration of nuclides.

Regarding the division of the internal boundaries of fault zones, Haneberg et al. (1999) reported that the fracture density in the rock of a fault zone is much greater than that of the host rock, where the fracture network of the fault zone is usually related to the direction of the main section of the fault. It is generally believed that fracture frequency can be used to characterize the influences of the fault on the surrounding rock mass (Haneberg et al. 1999; Lei et al. 2016; Ishibashi et al. 2016). Munier et al. (2003) argued that the fracture density can be  $4 \text{ m}^{-1}$ , a density which can act as the boundary between the fault zone and the host rock, and that it may reach  $9 \text{ m}^{-1}$  between the damage and core zones. Yang et al. (2006) and Gao et al. (2010) simulated the density at the midpoint of the joint and obtained the range of stability of the fault. Wang et al. (2013) carried out a geostatistical analysis of the fracture density based on a geographic information system (GIS) method and found that the fracture density values have obvious spatial autocorrelation and distribution characteristics. Guo et al. (2015) used Real Time Kinematic Global Positioning System (RTK-GPS) analysis to study the discontinuities of fractured rock masses and to categorized the studied regions. Lei et al. (2016) examined the joint densities and other statistical parameters of different parts of faults from a candidate rock mass in the vicinity of the Jijicao rock block and analyzed its geological structures. These authors found that when the distance exceeds the width of the fault damage zone, the mean joint density and trace length fluctuate within certain values.

However, it is not sufficient simply to determine the influence of a fault based on fractures to calculate the density. Differences in the spatial distribution, occurrence and aperture of fractures, as well as their influence on the seepage field, must be taken into consideration. It is also necessary to discuss the differences between the origin and characteristics of these fractures to assess the range of their influence and respect distance (RD). The damage zone between the core zone and the host rock must be considered. The RD which we propose here differs from that proposed by general engineering construction projects, and the core zone index includes the hydraulic conductivity of the factors that inhibit the migration of nuclides.

Although field surveying is an intuitive and reliable method for examining fault zones, it is limited by human activities and outcrop conditions, such that the measuring range can hardly cover the entire research area. Although the use of GIS facilitates the analysis, enabling a large volume of data to be obtained, the use of GIS makes it difficult to accurately examine the areas close to the nuclear waste repository. Therefore, fine manual analyses (e.g., scanline sampling,

mineral analysis) are performed. In the study reported here, we used both analyses reported in previous studies that were obtained from GPS data as well as manual field measurements. The location, distribution and other information about fracture spacing can be obtained from field measurements. Based on the statistically obtained distribution and the structural background information of the area, we have examined a representative set of fractures that has a significant influence on the seepage field according to the number of fractures and the degree of aperture. The influence range of the fault can be obtained by analyzing the overall fracture density with respect to the density of a representative set of joints. Additionally, by testing and analyzing field water pressure, we obtained a simplified conceptual model of changes in the spatial distribution of hydraulic conductivities at variable distances from the main section of the fault and the distribution of the seepage field of the fault and its surroundings. The methodology applied in this research is shown schematically in Fig. 1.

### Geological background

The studied site is the Jijicao rock block, which is located in the Beishan region of Gansu Province, China. It is one of the main candidate sites for the construction of a Chinese HLW repository. The studied site is located to the southwest of the Xinchang rock block and in the mid-east region of the Jijicao rock block. The northwest (NW) border of the rock block is 4 km long, and the northeast border is 3 km wide. Rocks are well exposed in outcrops in this region, which covers an area

of 12 km<sup>2</sup>. The main lithology is biotite monzonite granite. The tectonic deformation in this area is characterized by brittle fractures and joints, along with ductile shear deformation that has not been fully developed. Since the Indosinian–Yanshanian orogeny, the tectonic stress field has been dominated by left-lateral strike-slip movement; therefore, this area is characterized by the continuous development of low-angle fractures. The boundary faults in the east–west direction were thus cut and offset by the fault in the north–east (NE) direction. The long fractures and fracture zones are mainly characterized by steep dip angles. The rock block structure is primarily affected by the NE fault. The hydrogeological characteristics in this area are mainly controlled by the joints, fractures and faults in the rock mass and strata. The locations and orientations of seven main faults were determined based on interpretations of satellite images and observations of the surface (Fig. 2).

### Main fault zone

The seven types of faults in this region, as defined by Chen et al. (2009), are listed in Table 1. There are faults with tensional structures, extensional faults with tense-shearing, faults with compressive structures and faults with sinistral shear zones under tension. Among these, four faults (F1, F2, F4 and F6) are similar, although the west side of F4 is located further away from the other faults, and it has a longer distribution. Therefore, F4 was considered to be ideal for examining the range of influence of the fractures (Table 1; Fig. 2).

Fig. 1 Schematic of methodology. GPS Global Positioning System

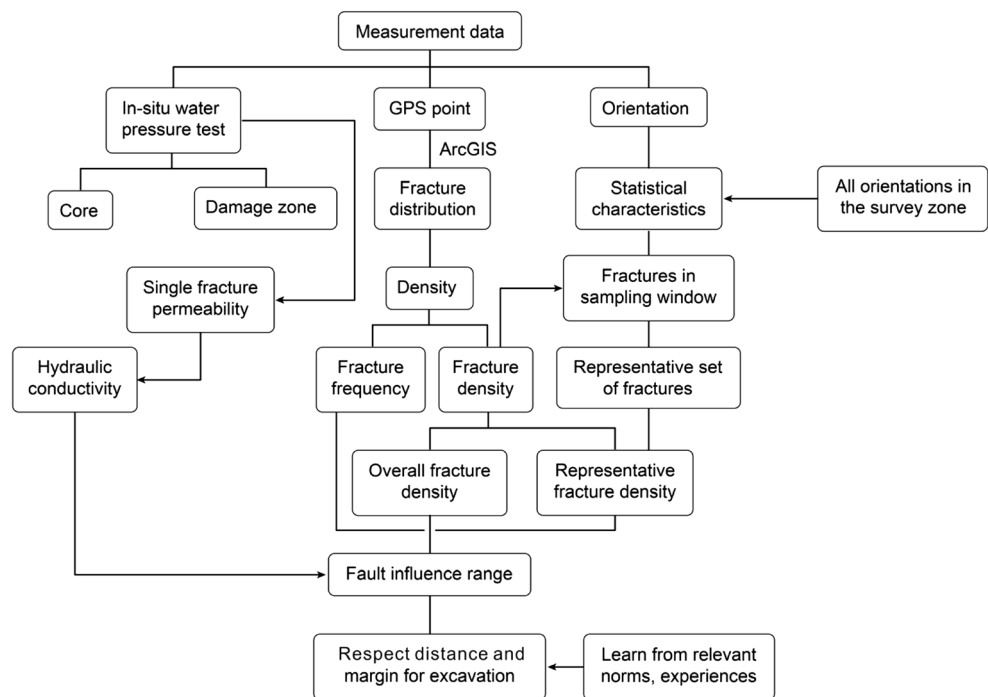
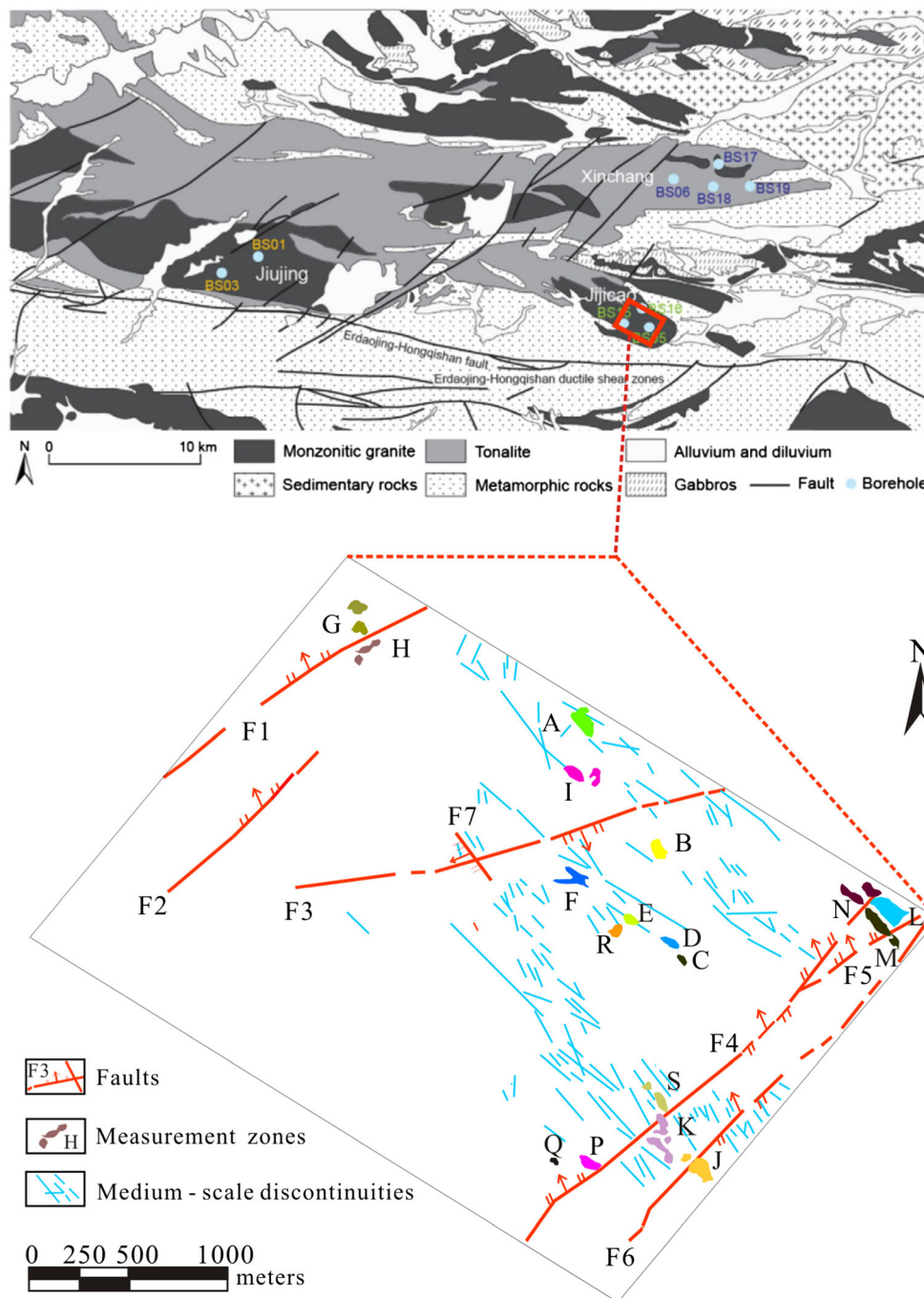


**Fig. 2** Locations of fracture measurements and relationships with faults in the Jijicao block. A–N, P–S Measured zones, F1–F7 primary faults. The discernible surface lengths of F1–F6 are over 1 km, while the length of F7 is < 1 km. Modified from Zhao et al. (2013), with permission



### F4 fault

The F4 fault is located in the eastern part of the studied area. It is one of the larger faults in the area and extends from north to south, with a total length of 2.9 km, and northward to the work area. While F6 is closer to F4 and its west side is more ideal for analysis, F6 is located farther away from the other large faults, and there is less impact due to these faults (see Fig. 2).

The general orientation of F4 is N40°W, with a dip of 300°–320° and a dip angle of 50°–60° in the fault

outcrops; hematitization is present, especially near the hanging wall of the fault, with a width of up to 2 m (see Fig. 3). Based on satellite images and field measurements, the measurement zone of the F4 fault was divided into three sections. The strike of the north section is 38.1°, that of the middle section is 48.5° and that of the south section is 38.2°. The measurement zone in the north section is denoted as N, and those in the middle section are denoted as P, S and K; see Fig. 2 (Guo et al. 2015).

**Table 1** Primary faults in the Jijicao block

Fault	Strike and dip angle of fault	Tectonic stress	Length (km)
F1	320° ∠ 66°	Tensional structure	1.8
F2	310° ∠ 65°	Tensional structure	1.5
F3	168° ∠ 57°	Extensional, with tense-shearing	2.9
F4	310° ∠ 55°	Tensional structure (in north and south parts), compressive structure (in middle)	2.9
F5	340° ∠ 75°	Sinistral shear zone under tension	1.2
F6	310° ∠ 56°	Compressive structure	2.65
F7	253° ∠ 76°	Tensional structure	0.45

## Fault structure

### Fault core

Mineral analysis revealed that mica and gypsum represent the main mineralogical components of the core of the fault. Close to the fractured zone, there are regions with weathered monzonite granite that contain small amounts of illite and weathered and dark diabase that contains chlorite. Particle size analysis showed that in the core of the fault samples, more than 30% of soil particles are > 2 mm in size and that more than 40% of soil particles are < 0.075 mm in size. The material distribution and mineral composition data thus indicate that the core should have low permeability. Moreover, many fractures are present on both sides of the fractured rock that have good connectivity and high permeability. Based on the analysis of the core samples and the categorization of the site, we determined the thickness of the fault core to be approximately 2 m.

Tomographic analysis of a sectional trench revealed the structure of the core (Fig. 4). There is fragile diabase near the hanging wall of the fault. The footwall is mainly composed of fractured granite. The fault core zone is mainly composed of chlorite, mud, hematite minerals and psephte. The core

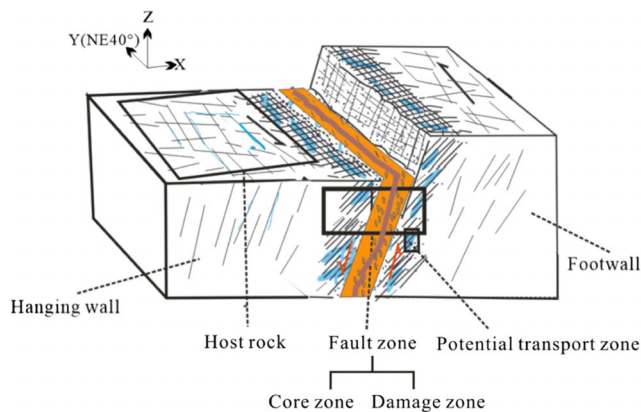
represents mud that has been mineralized by red hematite and is covered by loose Quaternary sediment.

### Fault damage zone

In this study, the Kamb contours of the poles are used to show the distribution of the orientation of the fault rupture zone (Kamb 1959; Vollmer 1995). In addition to analyzing the orientation of all fractures in the measurement zone, we also made measurements based on a uniform size window starting from the main section of the fault zone and extending outward equally. Fractures are planes that intersect the sampling window as line traces (Fig. 5). When a fracture intersects a circular window of finite size, the traces in which both ends are censored, one end is censored or both ends are observable with the sampling window are selected to analyze the orientations.

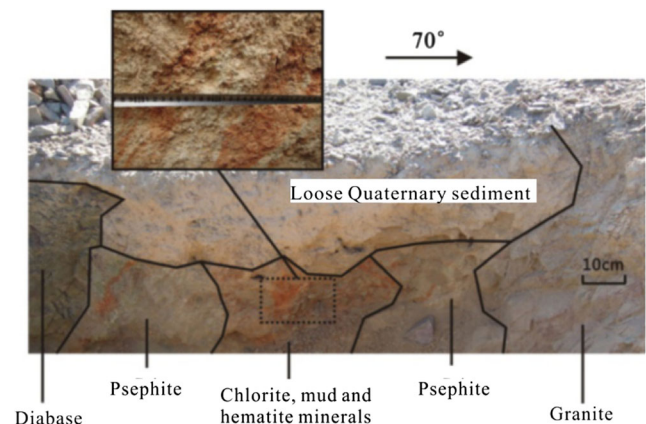
The initial purpose of the measured window is to calculate the trace midpoint density of the fracture. Further elaborations are provided in the section [Fracture density](#).

Figure 6 shows that although more samples are taken from all of the fractures in the measurement zone than density has been mapped, after using the sampling window, we created Schmidt and rose diagrams, which are more clear and intuitive. The reason for this methodology is because some areas



Schematic: not to scale

**Fig. 3** Sketch of the F4 fault. Arrows indicate the movement of each plate



**Fig. 4** Trench in core of the F4 fault

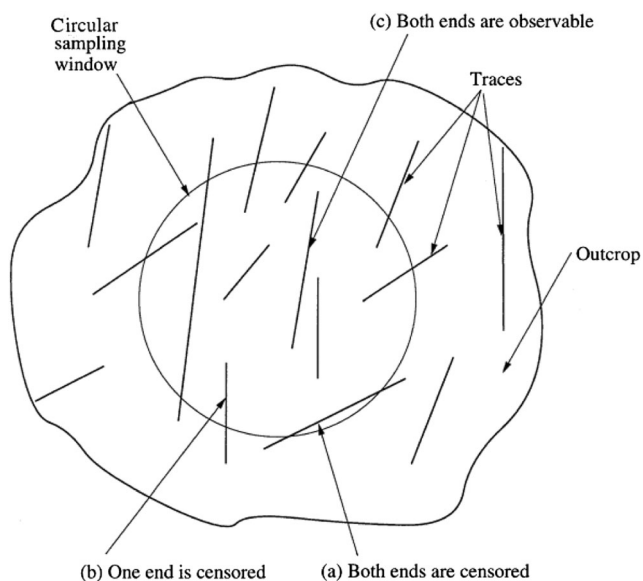


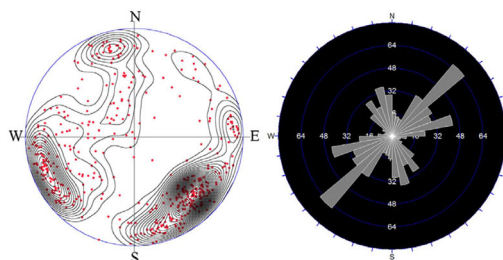
**Fig. 5** Fractures intersect a circular sampling window in three ways (Zhang and Einstein 1998)

are covered by loose Quaternary sediment. The weights of the orientations in the total distribution of different distances from

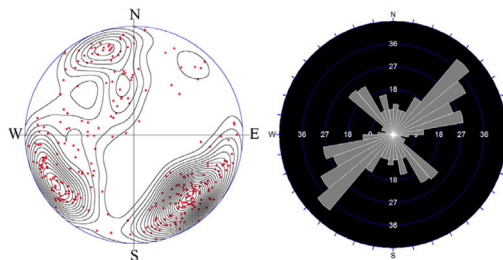
**Fig. 6** Fracture orientations in Zones S and K. **a.** Data presented with the Schmidt and rose diagrams of Zones S and K. **b.** Data filtered by window sampling with the Schmidt and rose diagrams of Zones S and K. **c.** Schmidt and rose diagrams after the modification of fracture trace lengths using window screening

the main plane of the fault are not consistent, and the actual statistically produced characteristics are distorted. Additionally, the Kamb method has the advantage that density is only minimally affected by the number of samples (Kamb 1959; Vollmer 1995; Zhou et al. 2012). Thus, the Schmidt diagram obtained after using the sampling window more accurately reflects the produced characteristics of the entire area, which is also supported by the rose diagram.

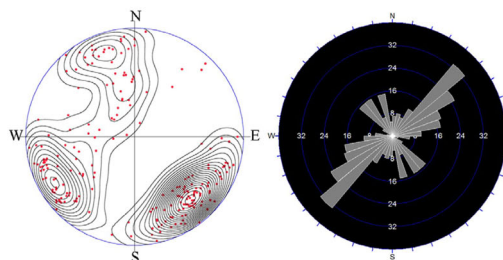
Additionally, because the fault damage zone is not strictly measured using the order of magnitude of the fracture trace length in this study, the correction of the fracture trace length in Zones S and K is carried out, in which fractures that are  $< 2$  m in length are removed. The results before and after this correction can be seen in the revised and unmodified chart and Schmidt diagram. The Schmidt diagram shows little changes, and there is no obvious deviation in the peak position due the trace length not being long in these measured zones. The difference between the longest and shortest trace length is an order of magnitude, and there are few fractures of  $< 2$  m in length, which is convenient for calculations as the fracture length of the measurement does not need to be modified.



**a.** Data presented with the Schmidt and rose diagrams of Zones S and K



**b.** Data filtered by window sampling with the Schmidt and rose diagrams of Zones S and K



**c.** Schmidt and rose diagrams after the modification of fracture trace lengths using window screening

### Representative set of fractures

The tectonic stress field affects movement, such that the fault zone often produces a series of shear faults that are parallel to the main plane of the fault (i.e. the principle slip zone). Moreover, during the relative movement of two plates, pinnate and shear fractures often develop on one or both sides of the fault. The acute angles of the pinnate fractures and the main fault section show the relative trend of the fault wall. In addition, a set of fractures with orientations similar to that of the main cross section developed due to the characteristics of the regional tectonic stress field (see Fig. 7).

Therefore, three representative sets of fractures are selected in Zone N. These sets are divided based on their strike direction, with an interval of 30°, and each set is established based on the principle a the dip direction difference of 180°. Based on these criteria, there are 119 samples in set A, 144 samples in set B and 122 samples in set C (see Table 2).

Using the same principle as in Zone N, two representative sets of fractures are selected in Zone P, including 130 samples in set A and 50 samples in set B. Two representative sets of fractures are selected from Zones S and K, including 90 samples in set A and 50 samples in set B (see Table 3).

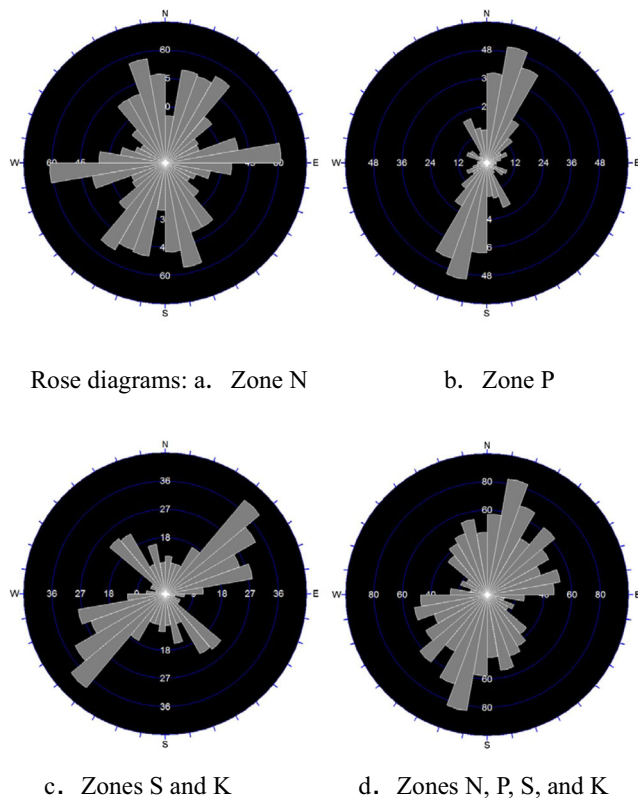


**Fig. 7** Fracture orientations in the target zones. **a–d** Rose diagrams of Zone N (a), Zone P (b), Zones S and K (c), Zones N, P, S and K (d)

**Table 2** Clustering based on orientation in Zone N

Zone N	Representative sets of fractures		
	Set A	Set B	Set C
Strike direction (°)	0–30	330–360	60–90
Dip direction 1 (°)	90–120	60–90	150–180
Dip direction 21 (°)	270–300	240–270	330–360

### Density

The node endpoints of the GPS-RTK data were exported as WGS84 coordinates and inputted into the GIS platform. After registration, the traces were generated and then the distribution of the fractures was obtained. Because fracture traces have line features, we can use a polyline or a straight line that is controlled by two or more points to represent a trace. By changing the trend of the fracture density, we can determine the effects of the NW plate on fault F4 (Zheng 2016).

### Fracture density

The endpoints of the trace lengths measured by the RTK analysis were projected onto the horizontal plane using ArcGIS, a GIS for working with maps and geographic information; a circular window was drawn from the equidistant position of the main section of F4 for calculations. For the fracture density calculations, the circular window sampling method proposed by Zhang and Einstein (1998) was used to estimate the mean trace length, and the calculation method of fracture density proposed by Mauldon (1998) was used. This method does not need to consider the distribution of orientations, and it does not require integration; it is only necessary to know the number of traces in which both ends are censored, one end is censored or both ends are observable.

**Table 3** Clustering based on orientation in Zones P, S and K

Zones	Representative sets of fractures	
	Set A	Set B
Zone P		
Strike direction (°)	0–30	330–360
Dip direction 1 (°)	90–120	60–90
Dip direction 2 (°)	270–300	240–270
Zones S and K		
Strike direction (°)	30–60	300–330
Dip direction 1 (°)	120–150	30–60
Dip direction 2 (°)	300–330	210–240

When a fracture trace intersects a circular window of finite size, this intersection may occur in one of three ways: (1) both ends are censored, (2) one end is censored and one end is observable or (3) both ends are observable, as is shown in Fig. 5. If the number of traces in each of the above three types are defined as  $N_0$ ,  $N_1$  and  $N_2$ , respectively, then the total number of traces,  $N$ , will be

$$N = N_0 + N_1 + N_2 \tag{1}$$

The mean trace length can be calculated using the following formula:

$$\mu = \frac{\pi(N + N_0 - N_2)}{2(N - N_0 + N_2)} c \tag{2}$$

where  $\mu$  is the mean trace length, and  $c$  is the window sampling radius.

The fracture density can be calculated using the following formula:

$$\lambda = \frac{N_1 + 2N_2}{2\pi c^2} \tag{3}$$

where  $\lambda$  is the fracture density of the trace midpoint, and  $c$  is the radius of the sample window.

In this paper, we first discuss the fracture density and trace length calculated using a circular window with different radiuses. As a result, when the radius is 5~6 m, there is little change in density, which is also supported by the findings obtained by Zhang and Einstein (1998) and Laslett (1982), who provided a formula to calculate trace lengths using different radiuses. Although, theoretically, the results are more likely accurate with a longer window radius, the width of the measurement zone is only 20~30 m. Therefore, when the radius of the window is

longer than half the width of the measurement zone, the density and trace results will deviate from the actual values and gradually decrease. For the convenience and accuracy of calculation, a window radius of 5 m is used for consistency with that used in a previous study (Fig. 8) (Li et al. 2011).

Figure 9 shows that the fracture density gradually significantly decreases with increasing distance from the main section of the fault in Zones N and P. From 10 to 100 m, the fracture density decreases by nearly an order of magnitude, from 0.6–0.8 to 0.1–0.2 n/m<sup>2</sup>. While this decreasing trend of fracture density is not obvious in Zones S and K, there are abnormally high density values at 90–100 m, mainly because the outcrops near the section of the main fault are covered by Quaternary sediments; thus, these are not good indicators of actual density changes.

Here, the trends of fracture density in Zones N and P are fitted.

The fitting results for Zone N are:

$$\lambda = 0.1290 + 1.9277 * e^{-L/18.4341}$$

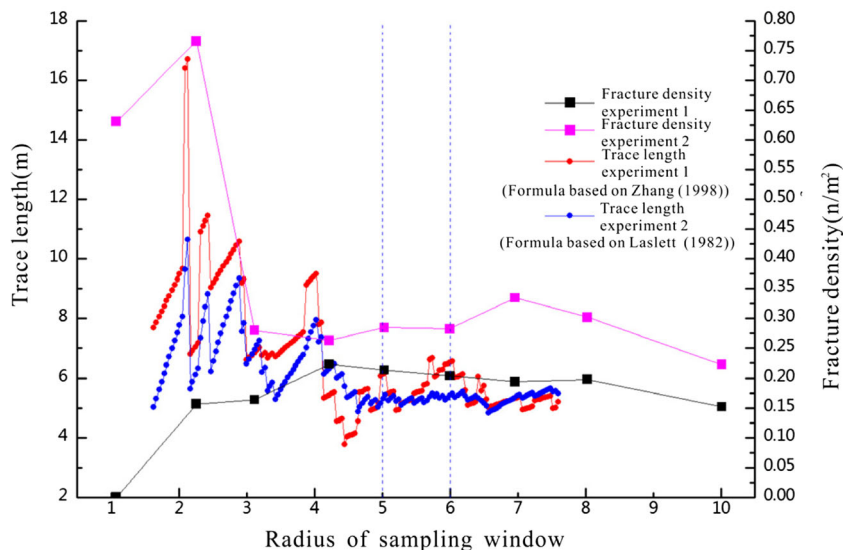
The fitting results for Zone P are:

$$\lambda = 0.1804 + 0.8505 * e^{-L/14.9937}$$

In both equations,  $\lambda$  is the density of the trace midpoint, and  $L$  is the distance from the main section of the fault.

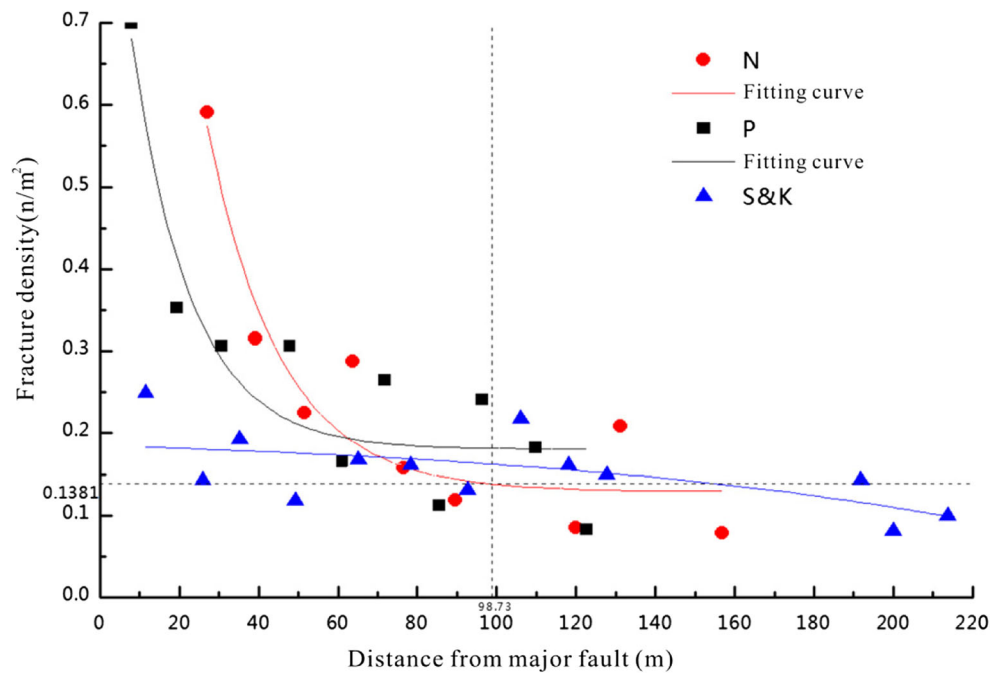
Examination of the trend of the fitting curves and the average fracture density obtained using multiple window sampling values in the homogenous zone reveals that the fault influence is 98.73 m in Zone N. The fracture density of Zone P may not converge to the threshold; however, near 100 m, the fitting curve is stable. Therefore, the

Fig. 8 Estimated density and trace length using different window radiuses





**Fig. 9** Density of trace midpoints in target zones



influence of the fault that extends to the NW boundary is set at 100 m, which is consistent with that proposed by Gao et al. (2010).

**Density of representative sets of fractures**

The calculated density of all fractures provides a range of values representing the influence of the fault, but these results do not take into account the differences between the different sets of fractures. Therefore, the differences in the spatial distribution of density, orientation and aperture are not reflected in the final spatial distribution. These results were based on section [Representative set of fractures](#), and the densities of the representative sets of fractures in Zones N and P were analyzed (Fig. 10).

The density distributions of the three sets of fractures in Zone N are not the same: set A becomes very dense at 65 m; set B does not become dense due to the abnormal elevation of the second half of the range; set C becomes dense at 150 m. In Zone P, set A becomes dense at 45 m; set B does not become dense due to the abnormally high elevation of the second half of the range. However, at 65 m, the set is already at a lower level. Therefore, in our analysis we consider the influence of set B also to be 65 m.

The density distribution of each set of fractures is different. This is closely related to the attributes of each set. Tension is applied to the set of fractures because the sliding drag along the main section of the fault is directly controlled by the fault. Therefore, with increasing distance from the main fault section, the attenuation of

fracture density becomes more effective. The densities of the other two sets, which are controlled by the regional stress field, attenuate more slowly.

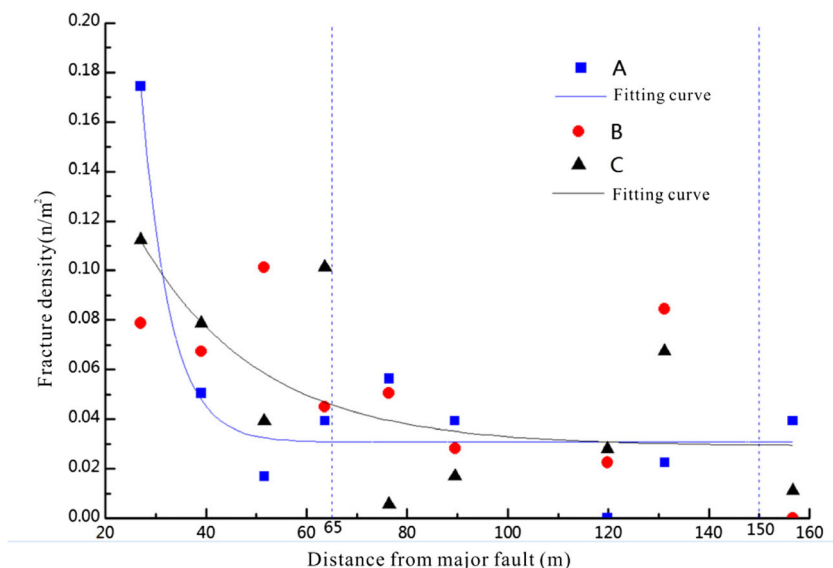
These sets of fractures exert important influences on seepage. Among them, the measured hydraulic conductivity values of the fractures in the representative set of tension fractures are larger, and they should thus have relatively strong impacts on seepage in the damage zone.

**Fracture frequency**

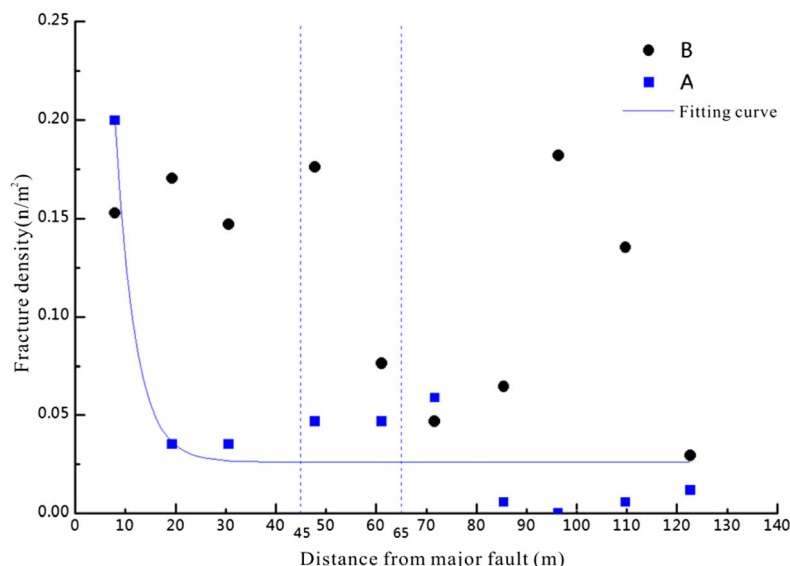
Restricted by the precision of GPS, outcrop conditions and other factors, the method described above cannot reliably define the density of the fracture pattern near the core of the fault. Therefore, to obtain the distribution of the fractures in the vicinity of the core, we selected an outcrop near the F4 trench in Zone P for detailed examination. The measurement of the field fracture frequency (denoted as the density of fractures in Fig. 11) was carried out by measuring the line. Based on these data, combined with field observations, we divided the measured area of F4 near the core of Zone P (denoted as C) into severely affected ( $H_L$ ), moderately affected ( $H_M$ ) and mildly affected ( $H_L$ ) areas. The locations of these three affected areas, as well as of the core of the fault and footwall (denoted as F), are shown in Fig. 11.

As shown in Fig. 12, moving from the areas that are very close to the fault towards the main section of the fault, the fracture frequency decreases from 50–60 n/m to < 10 n/m at a distance of 10 m from the main section of the fault. Values of

**Fig. 10** Density of trace midpoints of different sets of fractures in Zones N (a) and Zone P (b)



a. Density of different sets of fractures in Zone N



b. Density of different sets of fractures in Zone P

0–2.4 m are defined as very high fracture frequency values (70–35 n/m), values of 2.4 m–7.1 m are defined as moderate fracture frequency values (35–10 n/m) and values of 7.1 m–10 m represent the lower range of fracture frequency values (10–5 n/m).

Due to the limited length of the gouge and poor outcrop conditions, it was difficult to obtain measurements at a distance of 8.9 m from the main section of the fault; therefore, the follow-up fracture frequency was measured by GPS-RTK. The fracture frequency of the field survey line in Zone K is consistent with that measured using ArcGIS simulations, which demonstrates that this method

is robust. Using this method, we obtained the mixed-fracture frequency trend of Zone P (Fig. 13).

### Seepage characteristics

#### Experimental setup

Water pressure analysis was carried out on the severely influenced zone, homogenous zones and core of F4. In this analysis, a section of the borehole to be tested is sealed using inflatable plugs, which are called packers.

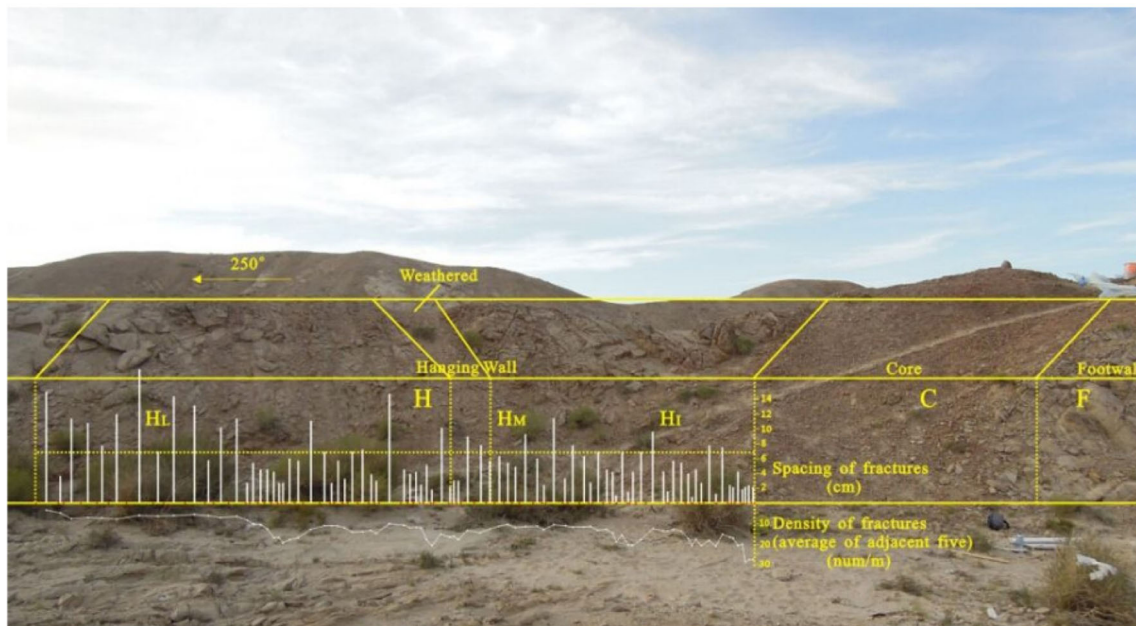


**Fig. 11** Segmentation of F4, hanging wall and Zone P. *C* Core of Zone P, *HI*, *HM*, *HL* measured areas of F4 which were severely affected, moderately affected and mildly affected, respectively, *F* footwall

The sealed borehole section is located either between a packer and the bottom of the borehole (i.e. a single packer test, as shown in Fig. 14) or between two packers (i.e. a double packer test). Water is then injected into the sealed section of the borehole under a defined pressure  $p$ . The pressure is increased in steps, and after the maximum pump pressure is reached, the pressure is decreased. The volume of water that escapes the test section (at a flow rate  $Q$ ) is measured at each pressure step. Using this method, we then obtained the hydraulic conductivity

values of the core of F4 and the damage zone and measured the hydraulic conductivity of a single fracture was measured.

**Analysis of results**

The results of the measured waterflood tests show that the Reynolds number is much lower than 2300. Therefore, Darcy’s law and the cubic law can be applied to assess the

**Fig. 12** Fracture frequency of Zone P

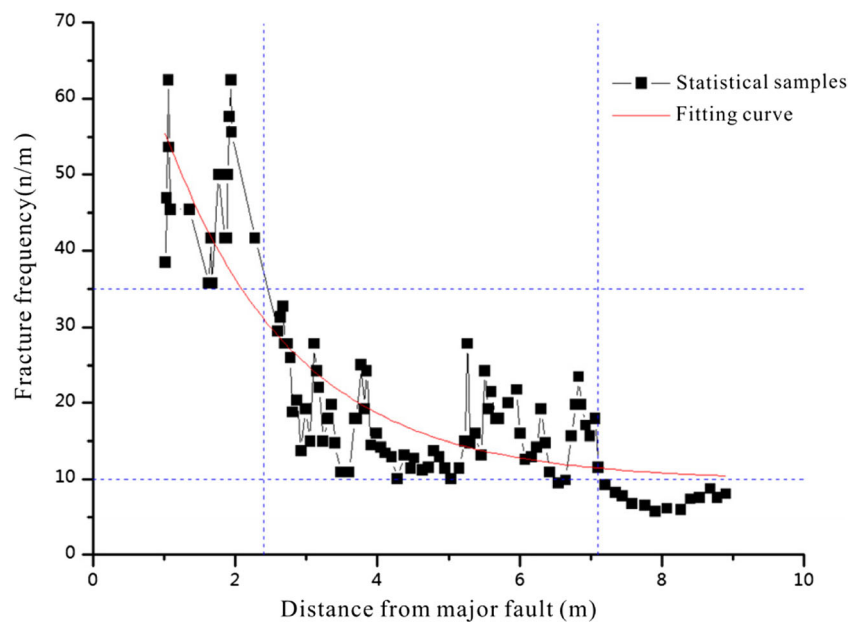
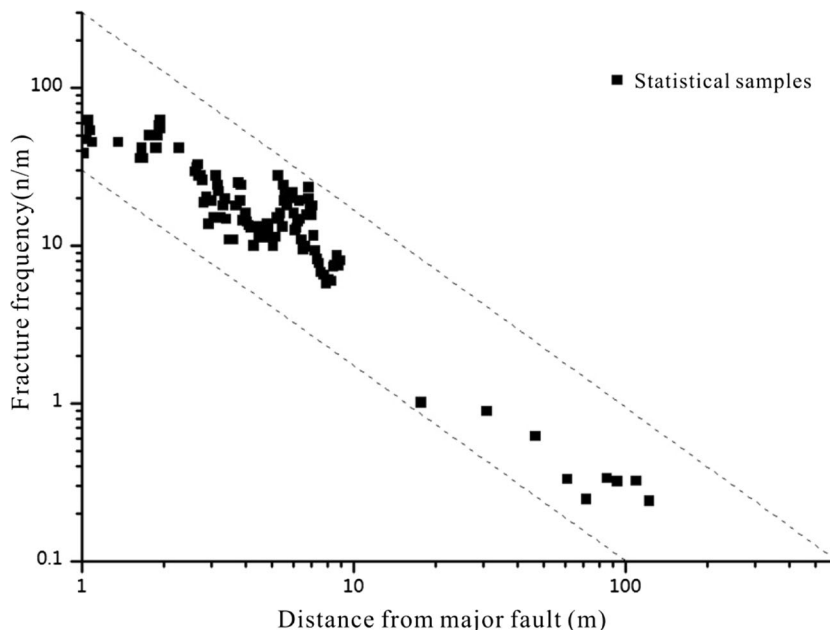


**Fig. 13** Fracture frequency of Zone P (together with those obtained using GIS)



water pressure of a hole of a single fracture in a homogeneous region.

The effective aperture of a single fracture can be calculated using the cubic law:

$$a = \sqrt[3]{\frac{12\cos\theta\gamma Q}{2\pi Rgt}} \tag{4}$$

where  $R$  is the drilling radius,  $t$  is the time,  $\gamma$  is a kinematic viscosity coefficient when the water temperature is 20 °C,  $\gamma$  is  $1.004 \times 10^{-6} \text{ m}^2/\text{s}$ ,  $Q$  is the flow rate and  $\theta$  is the fracture dip angle.

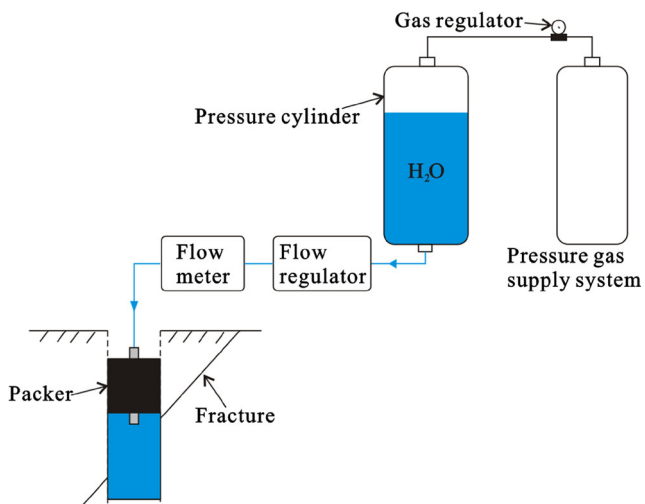


**Fig. 14** Schematic representation of the apparatus used in the water pressure test

The hydraulic conductivity  $K$  is given by:

$$K = \frac{q\cos\theta}{2\pi aH} \tag{5}$$

where  $q$  is the flow rate,  $\theta$  is the fracture dip angle,  $a$  is the degree of aperture and  $H$  is the water head difference.

The fault gouge and the fractured rock are considered to be porous media, and  $q \leq 10Lu$ ; thus, the results of the water pressure test can be obtained using the Babushkin formula (Li et al. 2007):

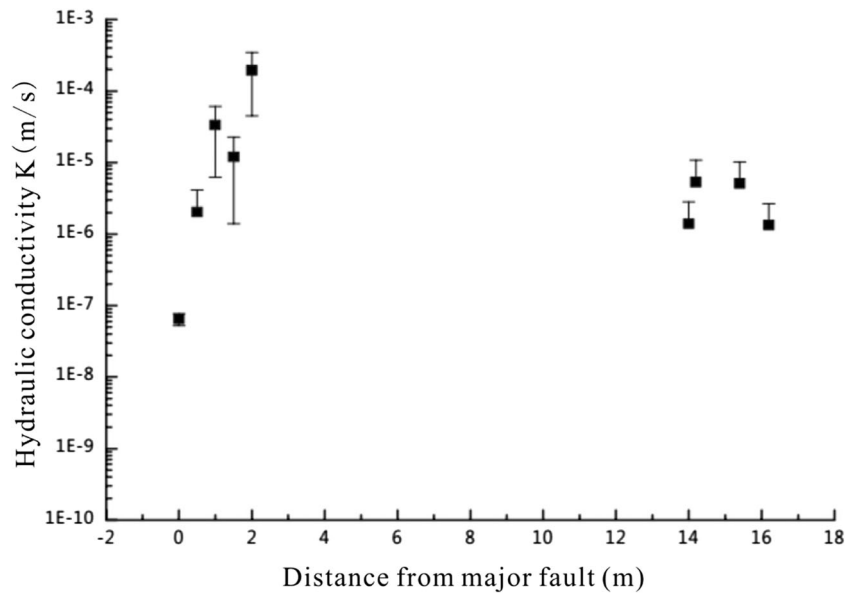
$$K = 0.525 \times \omega \times \lg \frac{aL}{R} \tag{6}$$

$$\omega = \frac{Q}{l \times p} \tag{7}$$

where  $K$  is the hydraulic conductivity (m/s),  $\omega$  is water absorption (L/ (min·m·Mpa)),  $L$  (m) is the length of the drill hole section,  $Q$ (L/ min) is the length  $l$ (m) of the tested section of water seeping into the rock per minute,  $p$ (Mpa) is pressure, and  $R$ (m) is the borehole radius. When the distance between the tested section and the aquifuge is greater than  $L$ ,  $a = 0.66$ .

The error bars represent the variability of the data (Fig. 15). The top and bottom of the short bars represent the addition or subtraction of the standard deviation, respectively; the longer the error bars are, the greater is the variability of the data. Figure 15 shows that Zone P, the fault core and host rock are less conductive when the damage zone is 10- to 100-fold more conductive due to the greater density of fractures, which is consistent with the results of mineral and grain size analysis.

**Fig. 15** Error bars of hydraulic conductivity. Error bars represent the variability of the data. See text for a more detailed explanation



**Calculation of equivalent hydraulic conductivity**

The altitude of the northwestern area is higher than those of the other hydrogeological areas in Beishan where orientations were measured. However, this difference is relatively minimal. As a result, the northwestern region is a groundwater supply area. The main stream of groundwater in this region flows from west to east, and the drainage area eventually flows into the Heihe River Basin. The supply and discharge conditions of the flow field can be seen in Fig. 16. Near F4, the groundwater flows from north to south. Considering that the medium of nuclear storage is silty sand, there is a greater fine content; thus, there are more fine particles filling in pores, and the permeability of the soil is low. Therefore, the water flow should be parallel to the orientation of the main fault section.

Therefore, in our study we examine a section that is perpendicular to the main section of the fault in Zone P of the measurement zone, and the following assumptions were made:

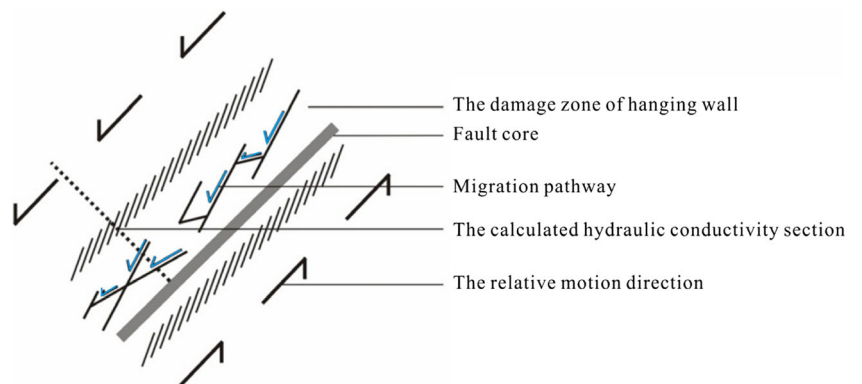
- (1) Each cross section is given the same hydraulic gradient ( $J$ );
- (2) The vertical thickness of the section is assumed to be uniform;
- (3) The orientation of the water diverted from a single fracture is neglected, and only the flow through the section is analyzed;
- (4) The vertical flow is neglected;
- (5) The fracture aperture and hydraulic conductivity in one set are the same.

In this section, the length of the segment is  $L$ ; assuming that there are  $N$  fractures in this section and that the cross-sectional area is  $A$ , then:

$$Q_L = \sum_{l=1}^n Q_l = \sum_{l=1}^n K_l A_l J = N K_e A_L J \tag{8}$$

To simplify  $N$  fractures into a set  $P$  based on their orientation, a set of fractures is formed because it has similar tectonic

**Fig. 16** Schematic diagram of hydraulic conductivity



characteristics. A set of fractures has the same hydraulic conductivity and aperture. Then, the following equation can be used to obtain the generalized hydraulic conductivity of a single fracture:

$$K_{es} = \left( \sum_{i=1}^n K_i A_i J \right) / NA_L J = \left( \sum_{i=1}^p K_i A_i N_i \right) / NA_L \quad (9)$$

If  $L$  is taken as the unit length, then  $N$  can be replaced by the fracture frequency  $f_i$  of a set of  $i$  fractures in that section, and the equivalent hydraulic conductivity of the length is used:

$$K_{ea} = \frac{\sum_{i=1}^p K_i A_i f_i}{\sum_{i=1}^p f_i A_i} f_a \quad (10)$$

We use the measured hydraulic conductivity and the aperture of a single representative fault to obtain the equivalent hydraulic conductivity of any unit length based on the change in fracture frequency over space. Zone P of F4 is calculated using this method (Fig. 17).

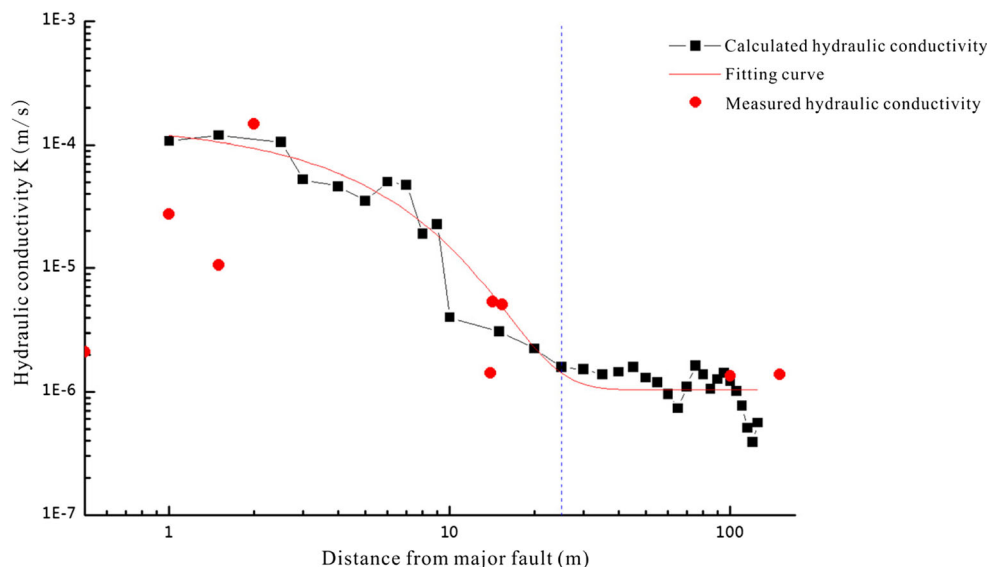
As shown in Fig. 17, the equivalent hydraulic conductivity and the measured hydraulic conductivity are similar. Both the fault core and host rock are less conductive, and the fractured zone is more conductive. There is a difference of two orders of magnitude between the two; the equivalent hydraulic conductivity shows stability at 25 m from the main section of the fault, and there is a minimum at 65 m, which corresponds well to the trend of fracture frequency in set B (which has a tensional structure) in Zone P, and the subsequent variation is small. These results show that the algorithm is reliable. In application, it is only necessary to confirm the hydraulic conductivity of the representative fractures in the field. By

measuring and calculating the locations and orientations of the fractures, the preliminary results of conductivity changes in this area can be obtained without performing extensive repeated penetration tests.

### Influence of fault zone on engineering

Some issues and concerns are usually involved in the process of underground construction, such as the identification of faults and their RD, as well as the assessment and reinforcement of stability after excavation (Zhang and Goh 2015; Li et al. 2017; Jin et al. 2018). Various countries have established specifications to consider RD, but many are based on the seismic considerations of buildings, which are not suitable for the research area and research objectives of the study reported here. During the implementation of their HLW disposal project, the SKB used RD and the margin for excavation (MFE) to control the deformation zone (Munier and Hökmark 2004). RD refers to the minimum allowable distance between the disposal hole and the deformation belt, and it is based on the influence of future seismic activity on storage tank safety. When the outcrop of the fault is larger than 3 km, the distance of the RD is set to 100 m. When the outcrop of the fault is less than 3 km, a disposal tunnel can be installed directly through the fault zone, but the nearest disposal hole must be located at a minimum distance equal to half the width of the deformation zone plus 5 m from the center of the deformation. The MFE is the minimum allowable distance between a tunnel or underground cavern and the deformation zone, which is the minimum distance between the outer edge of the hole and the center of the deformation belt. The specific value is half the width and variation of the deformation band,

Fig. 17 Measured and calculated results on hydraulic conductivity



plus the safety margin. For a fault that is less than 3 km, the safety margin is generally 5 m. However, if there is a stability problem, the safety margin is increased to 10 m, and if there is an infiltration problem, the safety margin must be increased to 20 m.

The SKB concluded that after grouting treatment, the hydraulic conductivity of the rock is often reduced to  $10^{-8}$  m/s in a rock mass with a hydraulic conductivity value of  $10^{-6}$  m/s. When the results of fracture density and seepage analyses are combined, a hydraulic conductivity threshold of  $10^{-8}$  m/s is considered appropriate. Considering the impact of conduct on a bandwidth of 25 m using a hydraulic conductivity of  $10^{-6}$  m/s, the safety margin is 5 m. Therefore, an MFE of 30 m is more appropriate in this case.

## Discussion

We report here our study of the NW range of the influence of the F4 fault. We found that both the host rock and the fault core are less conductive and that fractures are more developed and have a great influence on the seepage characteristics. Therefore, we assessed here the spatial distribution patterns and statistical characteristics of the orientation features in the damage zone and obtained the variations in the overall density of fractures with increasing distance from the main section of F4. Based on the number of fractures, as well as their orientations and apertures, specific sets of fractures related to the permeability of the fractured zone are classified, and their variability is examined. The water pressure analysis of these sets of fractures revealed that the tensional structure of F4 exerts a significant influence on its hydraulic conductivity. The changes in hydraulic conductivity allow the RD and MFE to be determined. Additionally, the changes in hydraulic conductivity provide a reference for a layout that will determine the disposal repository and can be used to calculate the storage capacity. A simplified method for estimating the hydraulic conductivity of similar sites is also proposed. The method we present here differs from a previous method that considers the density of all fractures in that our method considers the influence of tectonic history and geostress on the rock mass. Consequently, more accurate conclusions can be derived from using our method.

## Conclusions

Based on the research presented in this paper, the following conclusions can be made.

- (1). In granitic areas similar to the region studied here, the hydraulic conductivity values of the host rock and fault core are relatively low, and their hydrogeological

characteristics are mainly controlled by the fault damage zone.

- (2). If the overall fracture density is taken into account, the calculated range of the influenced area is too large, and reinforcements will be wasted; additionally, no direct relationship between fracture density and permeability has been defined. The analysis reported here shows that the tensional fracture frequency exerts a significant influence on hydraulic conductivity. However, the fracture frequency decreases rapidly with increasing distance from F4; compared with the fracture frequency of the other sets of fractures, the degree of tensional fracture frequency is not very obvious. If only tensional fracture frequency is considered, the results are not reliable.
- (3). The comprehensive comparison of the fracture frequency of tensional fractures with other representative sets reveals that the calculated hydraulic conductivity is stable at 25 m, which is consistent with the results of water pressure analyses. Accordingly, the MFE is 30 m.

**Acknowledgements** This study was financially supported by the National Basic Research Program of China (973 Program, No.2013CB036001), the National Defense Key Program (No. [2015]297), the Postdoctoral Innovative Talent Support Program of China (BX201700113), the National Natural Science Foundation of China (41702326), the Natural Science Foundation of Jiangxi Province (20171BAB206022), and the State Key Laboratory for GeoMechanics and Deep Underground Engineering, China University of Mining & Technology (SKLGDUEK1703). The support received for this project from the Beijing Research Institute of Uranium Geology is greatly appreciated.

## References

- Agosta F, Prasad M, Aydin A (2007) Physical properties of carbonate fault rocks, Fucino basin (Central Italy): implications for fault seal in platform carbonates. *Geofluids* 7(1):19–32
- Andersson J (1999) SR 97: Data and data uncertainties, compilation of data and evaluation of data uncertainties for radio-nuclide transport calculations. SKB Technical Report TR-99-09. Swedish Nuclear Fuel and Waste Management Co. (SKB), Stockholm
- Bauer JF, Meier S, Philipp SL (2015) Architecture, fracture system, mechanical properties and permeability structure of a fault zone in lower Triassic sandstone, upper Rhine graben. *Tectonophysics* 647–648:132–145
- Bruhn RL, Parry WT, Yonkee WA, Thompson T (1994) Fracturing and hydrothermal alteration in normal fault zones. *Pure Appl Geophys* 142(3–4):609–642
- Caine JS, Evans JP, Forster CB (1996) Fault zone architecture and permeability structure. *Geology* 24:1025–1028
- Chen L, Wang J, Zong ZH, Liu J, Su R, Guo YH, Jin YX, Chen WM, Ji RL, Zhao HG, Wang XY, Tian X, Luo H, Zhang M (2015) A new rock mass classification system Q HLW for high-level radioactive waste disposal. *Eng Geol* 190(2):33–51
- Chen WM, Wang J, Jin YX, Zhao HG, Li YF, Zhong X (2009) Geological feature of Jijicao block in Beishan pre-selected area for the disposal of high level radioactive waste. *World Nucl Geosci* 26(2):109–113,118

- Chester FM, Logan JM (1986) Implications for mechanical properties of brittle faults from observations of the punchbowl fault zone, California. *Pure Appl Geophys* 124(1–2):79–106
- Doughty PT (2003) Clay smear seals and fault sealing potential of an exhumed growth fault, Rio Grande rift, New Mexico. *AAPG Bull* 87(3):427–444
- Evans JP, Forster CB, Goddard JV (1997) Permeability of fault-related rocks, and implications for hydraulic structure of fault zones. *J Struct Geol* 19(11):1393–1404
- Fisher QJ, Knipe RJ (1998) Fault sealing processes in Siliclastic sediments, in faulting, fault sealing and fluid flow in hydrocarbon reservoirs. *Geol Soc London Spec Publ* 147:117–134
- Gao J, Yang CH, Wang GB (2010) Discussion on zoning method of structural homogeneity of rock mass in Beishan of Gansu province. *Rock Soil Mech* 31(2):588–592, 598
- Guo L, Li XZ, Zhou YY, Zhang YS (2015) Generation and verification of three-dimensional network of fractured rock masses stochastic discontinuities based on digitalization. *Environ Earth Sci* 73:7075–7088
- Haneberg WC, Mozley PS, Moore JC, Goodwin LB (1999) Fault zone architecture and fluid flow: insights from field data and numerical modeling. In: Haneberg WC, Mozley PS, Moore JC, Goodwin LB (eds) *Faults and subsurface fluid flow in the shallow crust*. American Geophysical Union, Washington D.C., pp 101–127
- Ishibashi M, Yoshida H, Sasao E, Yuguchi T (2016) Long term behavior of hydrogeological structures associated with faulting: an example from the deep crystalline rock in the Mizunami URL, Central Japan. *Eng Geol* 208:114–127
- Jin DL, Yuan DJ, Li XG, Zheng H (2018) An in-tunnel grouting protection method for excavating twin tunnels in beneath an existing tunnel. *Tunn Undergr Space Tech* 71:27–35
- Kamb WB (1959) Ice petrofabric observations from blue Glacier, Washington, in relation to theory and experiment. *J Geophys Res* 64(11):1891–1909
- Knipe RJ (1993) The influence of fault zone processes and diagenesis on fluid flow. In: Horbury AD, Robinson AG (eds) *Diagenesis and basin development*. AAPG Stud Geol 36:135–151
- Knipe J, Lloyd GE (1994) Microstructural analysis of faulting in quartzite, Assynt NW Scotland: implications for fault zone evolution. *Pure Appl Geophys* 143(1–3):229–254
- Laslett GM (1982) Censoring and edge effects in areal and line transect sampling of rock joint traces. *Math Geol* 14(2):125–140
- Lee YM, Jeong J (2011) Evaluation of nuclide release scenarios for a hypothetical LILW repository. *Prog Nucl Energy* 53(6):760–774
- Lee YM, Choi HJ, Kim K (2016) A preliminary comparison study of two options for disposal of high-level waste. *Prog Nucl Energy* 90:229–239
- Lei GW, Yang CH, Wang GB, Chen SW, Wei X, Huo L (2016) The development law and mechanical causes of fault influenced zone. *Chin J Rock Mech Eng* 35(2):231–241
- Li P, Lu WX, Yang W, Li J (2007) Determination of hydraulic conductivity tensor of fractured rock mass in reservoir. *J Hydr Eng* 38(11):1393–1396
- Li SC, Liu B, Xu XJ, Nie LC, Liu ZY, Song J, Sun HF, Chen L, Fan KR (2017) An overview of ahead geological prospecting in tunnelling. *Tunn Undergr Space Tech* 63:69–94
- Li XZ, Zhou YY, Wang ZT, Zhang YS, Guo L, Wang YZ (2011) Effects of measurement range on estimation of trace length of discontinuities. *Chin J Rock Mech Eng* 30(10):2049–2056
- Matonti C, Lamarche J, Guglielmi Y, Marié L (2012) Structural and petrophysical characterization of mixed conduit/seal fault zones in carbonates: example from the Castellas fault (SE France). *J Struct Geol* 39(3):103–121
- Mauldon M (1998) Estimating mean fracture trace length and density from observations in convex windows. *Rock Mech. Rock Engng.* 31(4):201–216
- McCaig AM (1988) Deep fluid circulation in fault zones. *Geology* 16(10):867–870
- McGrath AG, Davison I (1995) Damage zone geometry around fault tips. *J Struct Geol* 17(7):1011–1024
- Micarelli L, Benedicto A, Wibberley CAJ (2006) Structural evolution and permeability of normal fault zones in highly porous carbonate rocks. *J Struct Geol* 28(7):1214–1227
- Molli G, Corceci G, Vaselli L, Ottia G, Cortopassi A, Dinelli E, Mussi M, Barbieri M (2010) Fault zone structure and fluid-rock interaction of a high angle normal fault in Carrara marble (NW Tuscany, Italy). *J Struct Geol* 32:1334–1348
- Munier R, Hökmark H (2004) Respect distances. Rationale and means of computation. SKB R-04-17. Swedish Nuclear Fuel and Waste Management Co. (SKB), Stockholm
- Munier R, Stenberg L, Stanfors R, Milnes AG, Hermanson J, Triumf C-A (2003) Geological site descriptive model. A strategy for model development during site investigations. SKB R-03-07. Swedish Nuclear Fuel and Waste Management Co. (SKB), Stockholm
- Pere T, Aro S, Mattila J, Ahokas H, Vahtinen T, Wikström L (2012) Layout determining features, their influence zones and respect distances at the olkiluoto site. POSIVA report 2012–21. Posiva Oy, Olkiluoto
- Rawling GC, Goodwin LB, Wilson JL (2001) Internal architecture, permeability structure, and hydrologic significance of contrasting fault-zone types. *Geology* 29(1):43–46
- Sibson RH (1996) Structural permeability of fluid-driven fault-fracture meshes. *J Struct Geol* 18(8):1031–1042
- Storti F, Billi A, Salvini F (2003) Particle size distributions in natural carbonate fault rocks: insights for non-self-similar cataclasis. *Earth Planet Sc Lett* 206(1):173–186
- Svensk Kärnbränslehantering AB (2011) Long-term safety for the final repository for spent nuclear fuel at Forsmark: main report of the SR-Site project. SKB Report TR-11-01. Swedish Nuclear Fuel and Waste Management Co. (SKB), Stockholm
- Vollmer FW (1995) C program for automatic contouring of spherical orientation data using a modified Kamb method. *Comput Geosci* 21(1):31–49
- Walker D, Gylling B (1998) Site-scale groundwater flow modelling of Aberg. SKB Technical Report TR 98–23. Swedish Nuclear Fuel and Waste Management Co. (SKB), Stockholm
- Walker D, Gylling B (1999) Site scale groundwater flow modelling of Ceberg. SKB Technical Report TR 99–13. Swedish Nuclear Fuel and Waste Management Co. (SKB), Stockholm
- Walker RJ, Holdsworth RE, Imber J, Faulkner DR, Armitage PJ (2013) Fault zone architecture and fluid flow in interlayered basaltic volcanoclastic-crystalline sequences. *J Struct Geol* 51(6):92–104
- Wang P, Li XZ, Zhang YS, Zhao XB, Zhou YY, Fu AX, Wu WB (2013) Gis based geostatistical analysis of fracture density of granite rock in Beishan area Gansu Province. *J Eng Geol* 21(1):115–122
- Yang CH, Bao HT, Wang GB, Mei T (2006) Estimation of mean trace length and trace midpoint density of rock mass joints. *Chin J Rock Mech Eng* 25(12):2589–2592
- Yoshida H, Takeuchi M, Metcalfe R (2005) Long-term stability of flow-path structure in crystalline rocks distributed in an orogenic belt, Japan. *Eng Geol* 78(3):275–284
- Yoshida H, Maejima T, Nakajima S, Nakamura Y, Yoshida S (2013a) Features of fractures forming flow paths in granitic rock at an LPG storage site in the orogenic field of Japan. *Eng Geol* 152:77–86
- Yoshida H, Metcalfe R, Ishibashi M, Minami M (2013b) Long-term stability of fracture systems and their behaviour as flow paths in uplifting granitic rocks from the Japanese orogenic field. *Geofluids* 13(1):45–55
- Yoshida H, Nagatomo A, Oshima A, Metcalfe R (2014) Geological characterisation of the active Atera fault in Central Japan: implications for defining fault exclusion criteria in crystalline rocks around radioactive waste repositories. *Eng Geol* 177(14):93–103



- Zhang WG, Goh ATC (2015) Numerical study of pillar stresses and interaction effects for twin rock caverns. *Int J Numer Anal Met* 39(2):193–206
- Zhang L, Einstein HH (1998) Estimating the mean trace length of rock discontinuities. *Rock. Mech Rock Eng* 31(4):217–235
- Zhao XG, Wang J, Cai M, Ma LK, Zong ZH, Wang XY, Su R, Chen WM, Zhao HG, Chen QC, An QM, Qin XH, Ou MY, Zhao JS (2013) In-situ stress measurements and regional stress field assessment of the Beishan area, China. *Eng Geol* 163(16):26–40
- Zheng J (2016) Digital method to acquire geometric parameters of discontinuity and research on 3D network model. Nanjing University of Science & Technology, Nanjing
- Zhou YY, Li XZ, Guo L (2012) Delineation of major joint sets for Gansu Beishan area. *J Disas Prev Mitig Eng* 32(Supp 2):188–193. <http://www.doc88.com/p-1816945615062.html>